Determination of thermal expansion, defect formation energy, and defect-induced strain of α-U via *ab initio* molecular dynamics

Benjamin Beeler [1,2,*]**, Khadija Mahbuba** [1]**, Yuhao Wang** [3]**, and Andrea Jokisaari** [2]

[1]*North Carolina State University, Raleigh, NC 27607*
[2]*Idaho National Laboratory, Idaho Falls, ID 83415*
[3]*University of Michigan, Ann Arbor, MI 48109*

Correspondence*:
2500 Stinson Dr, Raleigh, NC, 27607
bwbeeler@ncsu.edu

2 ABSTRACT

Uranium (U) is often alloyed with molybdenum (Mo) or zirconium (Zr) in order to stabilize its high-temperature body-centered cubic phase for use in nuclear reactors. However, in all metallic fuel forms, the α phase of U remains in some fraction. This phase decomposition due to temperature or compositional variance can play an outsized role on fuel performance and microstructural evolution. Relatively little is known about fundamental point defect properties in α-U at non-zero temperatures, from either computational or experimental studies. This work performs the first thorough evaluation of the α phase of U via *ab initio* molecular dynamics (AIMD). A number of thermophysical properties are calculated as a function of temperature, including equilibrium lattice parameters, thermal expansion, and heat capacity. These results indicate a two-region behavior, with the transition at 400 K. The thermal expansion/contraction in the *a/b* direction occurs rapidly from 100 K up to 400 K, after which a more linear and gradual change in the lattice constant takes place. The volumetric expansion matches experiments quantitatively, but the individual lattice constant expansion only matches experiments qualitatively. Point defect formation energies and induced lattice strains are also determined as a function of temperature, providing insight on defect populations and the fundamentals of irradiation growth in α-U. Interstitials induce significantly more strain than vacancies, and the nature of that strain is highly dependent on the individual lattice directions. The direction of point **defect-induced** lattice strain is contrary to the irradiation growth behavior of α-U. This work shows that isolated point defects cannot be the primary driving force responsible for the significant **irradiation-induced** growth of α-U observed experimentally.

Keywords: alpha uranium, ab initio molecular dynamics, point defects, lattice strain, fuel swelling

1 INTRODUCTION

Uranium (U) is an actinide element exhibiting delocalized f-electrons that exists in three solid phases: α (face-centered orthorhombic), β (tetragonal with a 30 atom unit cell) and γ (body-centered cubic) Yoo et al. (1998). Below 935 K, U exists in the α phase Söderlind (1998). Although uranium is alloyed with Mo or Zr in order to stabilize the preferred body-centered cubic phase at lower temperatures, most notably for

28 nuclear fuel applications, the α phase persists either in decomposed phase regions (as in the case of U-Mo
29 fuel) or in the **low-temperature** periphery of the fuel slug (as in the case of U-Zr type fuel). Because of
30 its unique crystal structure, α-U exhibits anisotropic material properties, for example, thermal expansion
31 Lloyd and Barrett (1966) and elastic constants Fisher and McSkimin (1958). One relevant behavior is
32 the anisotropic irradiation growth of α-U Leggett et al. (1963), which can lead to the tearing along grain
33 boundaries and the formation of crystallographically aligned pores. These porosities are believed to form
34 due to the interaction of lattice defects and stresses induced by irradiation and a temperature gradient
35 and result in significant volume changes of α-U Leggett et al. (1963); Paine and Kittel (1958). A full
36 understanding of the relationship between point defects, lattice strains, and the generation of pores, has not
37 been established either experimentally or via computational methods. However, a number of computational
38 studies have been performed into fundamental properties of uranium Jokisaari (2020).

39 Density functional theory (DFT) is an essential part of computational materials science, addressing a
40 variety of problems in materials design and processing on a fundamental level. Several examinations of
41 U via DFT have been performed on its orthorhombic and body-centered cubic (bcc) structures. Taylor
42 Taylor (2008) used a projector augmented wave (PAW) pseudo-potential to calculate the lattice constants
43 of α-U and γ-U along with the bulk modulus of both phases and the surface energy of a single surface
44 in α-U. Xiang, *et al.* Xiang et al. (2008) also utilized a PAW pseudo-potential to perform an analysis of
45 lattice constants in the α and γ phases, as well as an analysis of defects in γ-U. Beeler, *et al.* calculated
46 the lattice constants and elastic constants of α, β and γ-U Beeler et al. (2013), in addition to the point
47 defect properties in both α and γ-U Beeler et al. (2010). Huang and Wirth Huang and Wirth (2011, 2012)
48 calculated intrinsic and extrinsic point defect formation energies and migration barriers in α-U. These DFT
49 investigations showed a general, if imperfect, agreement with the experimental bulk moduli, lattice and
50 elastic constants, and vacancy formation energy Yoo et al. (1998); Barrett et al. (1963); Matter et al. (1980).

51 Key areas lacking from the DFT-based literature on α-U include an analysis of temperature-dependent bulk
52 properties, including thermal expansion and heat capacity, and temperature-dependent defect properties.
53 Extrapolation of 0 K properties to compare to elevated temperature experiments can be ill-advised,
54 particularly for complex crystal structures or for point defects. However, *ab initio* molecular dynamics
55 (AIMD) allows for quantum mechanical-based calculations to be performed at non-zero temperatures.
56 AIMD has been utilized to study a variety of systems including liquid phase diffusion in Al-Si Manga and
57 Poirier (2018), **the** adsorption energy of Fe on TiN surfaces Wang et al. (2010), NaCl dissolution in water
58 Timko et al. (2010) and finite temperature phonon dispersion curves in bcc Zr and bcc Li Hellman et al.
59 (2011). Hood, *et al.* Hood et al. (2008) have previously utilized AIMD to study the equation of state of
60 U and the variation in density of states for the liquid phase of U at two unique temperatures. Hood, *et al.*
61 utilized a unique pseudo-potential that was presented in that same manuscript Hood et al. (2008). Soderlind,
62 *et al.* Söderlind et al. (2012) utilized self-consistent *ab initio* lattice dynamics (SCAILD) to study the
63 **high-temperature** stabilization of the γ-U phase by calculating phonon modes at 1100 K. There have
64 been several investigations of the free energy via the **temperature-dependent** effective potential (TDEP)
65 technique Hellman et al. (2013); Ladygin et al. (2020); Kruglov et al. (2019); Bouchet and Bottin (2017);
66 Castellano et al. (2020), and one recent AIMD investigation into the defect formation energies in γ-U at
67 high temperatures Beeler et al. (2020). Despite numerous **investigations** into metallic uranium, AIMD
68 has not been deployed to study **temperature-dependent** properties of α-U, such as thermal expansion or
69 defect formation energies.

70 In this work, AIMD simulations are performed to calculate the equilibrium volume of α-U as a function of
71 temperature. Utilizing these equilibrium volumes, the three lattice constants of α-U are determined, yielding

72 anisotropic thermal expansion calculations. Additionally, point defect formation energies for interstitials
73 and vacancies are calculated as a function of temperature. The lattice strain from the introduction of these
74 point defects is calculated, providing insight into the fundamental stages of irradiation growth. This is the
75 first AIMD investigation of point defects in α-U.

2 MATERIALS AND METHODS

76 Systems are investigated using the Vienna *ab initio* Simulation Package (VASP) Kresse and Hafner (1993,
77 1994); Kresse and Fürthmuller (1996a,b). The projector augmented wave (PAW) method Blöchl (1994);
78 Kresse and Joubert (1999) is utilized within the density functional theory Hohenberg and Kohn (1964);
79 Kohn and Sham (1965) framework. Calculations are performed using the Perdew-Burke-Ernzerhof (PBE)
80 Perdew et al. (1996, 1997) generalized gradient approximation (GGA) density functional implementation
81 for the description of the exchange-correlation. A uranium PAW pseudo-potential with the $6s^2 6p^6 5f^3 6d^1 7s^2$
82 valence electronic configuration and a core represented by [Xe, 5d, 4f] is utilized. Methfessel and Paxton's
83 smearing method Methfessel and Paxton (1989) of the first order is used with a width of 0.1 eV to
84 determine the partial occupancies for each **wavefunction**. A Monkhorst-Pack Monkhorst and Pack (1976)
85 1x1x1 k-point mesh was utilized for Brillouin zone sampling. Uranium is assumed to be non-magnetic, in
86 accordance with both experiments Lide (2000) and previous simulations Beeler et al. (2013), and as such
87 calculations are non-spin-polarized. The Hubbard U term is not applied to the f electrons, in accordance
88 with previous computational studies that utilized DFT on α-U Huang and Wirth (2011, 2012); Taylor
89 (2008); Beeler et al. (2013). The precision is set to normal and the energy cutoff is increased to 300 eV.
90 The electronic self-consistent loop exit criterion is set to 10^{-4} and the precision for projectors in real
91 space is increased to -10^{-4}. A 180 atom supercell (5x3x3 unit cells) is utilized for all simulations. Such a
92 supercell is sufficiently large to preclude defect-defect interactions **Huang and Wirth (2011)**. Dynamics
93 were carried out in the NpT ensemble with Parinello-Rahman dynamics and a Langevin thermostat to
94 control temperature. The temperature range investigated is from 100 K to 800 K, in increments of 100 K,
95 to span nearly the entire range of stability of the α phase of U. The Langevin friction coefficient for both
96 the atomic and lattice degrees-of-freedom was set to 5 ps^{-1}, with a fictitious mass for the lattice degrees of
97 freedom of 500 amu. The timestep is set to 2.0 fs, and the initial structures are equilibrated at the target
98 temperature for 8 ps. The trajectories of the total supercell energy, pressure, and individual lattice vectors
99 are analyzed as a function of timestep to ensure that an equilibrated state has been reached and each of
100 these quantities **is** oscillating around a given value, with the pressure oscillating around zero. Subsequently,
101 the simulations are further equilibrated for 2000 timesteps (4 ps) for the determination of equilibrium
102 properties. In order to obtain average properties over the *ab initio* molecular dynamics simulation, the
103 energies and lattice constants for the final 1500 timesteps (3 ps) are extracted and averaged. **To** ensure
104 statistical significance of the results, ten unique simulations are performed for each simulation setup. An
105 example trajectory of the individual supercell lattice constants **as a function of** time at 300 K is shown in
106 Fig. 1. The standard deviation in the a, b, and c equilibrium lattice constants from this single simulation are
107 0.01 Å, 0.02 Å and 0.01 Å, respectively. It should be emphasized that this was a single simulation, and ten
108 such simulations were performed to obtain the averaged equilibrium structures and energies. Error bars are
109 excluded from figures in the results that pertain to lattice constants, due to the small deviations observed in
110 the dataset.

111   The thermal expansion is calculated both for individual lattice constants, and as a volume averaged value,
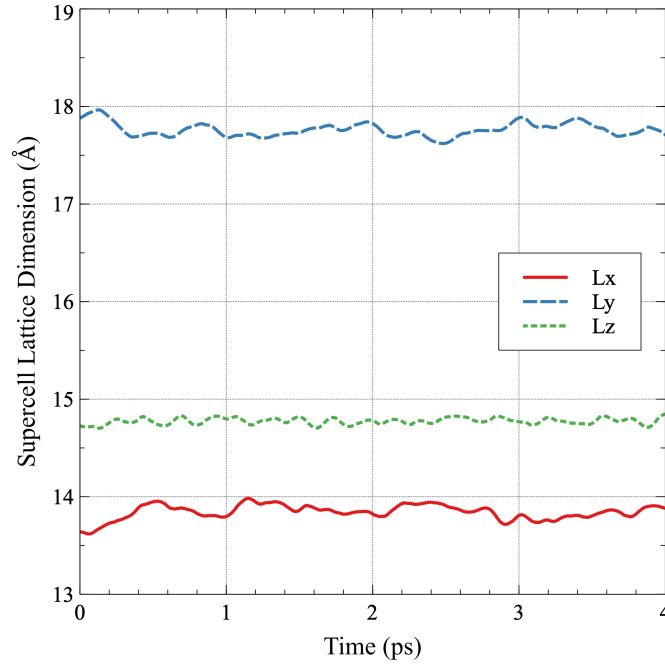112 via equation 1:

Figure 1. The supercell lattice dimensions as a function of time for α-U. Each dimension is averaged over the final 3 ps to obtain the average lattice constant in the simulation.

$$\alpha = \frac{L - L_0}{L_0} \tag{1}$$

113　where α is the thermal expansion, and L is the length of the individual lattice constant or averaged lattice
114　constant **(cube root of the volume)** at a given temperature, and L_0 is the reference length at a given
115　temperature. The formation energy of point defects is calculated via equation 2:

$$E_f = E^* - \frac{n \pm 1}{n} \times E_0 \tag{2}$$

116　where E^* is the energy of a system with a defect (with n ± 1 atoms), *n* is the number of atoms in the
117　defect-free system and E_0 is the energy of a defect-free system with *n* atoms. Equation 2 utilizes (*n* + 1) for
118　interstitials and (*n* - 1) for vacancies. The molar heat capacity is determined from equation 3:

$$C_P = \left(\frac{\delta H}{\delta T} \right)_P \tag{3}$$

119　where H is the enthalpy (potential plus kinetic energy), T is the temperature, and it is emphasized that this
120　is determined for a constant pressure, which in these simulations is zero pressure. The total heat capacity is
121　a sum of the lattice (Eq. 3) and the electronic components of the heat capacity. The electronic heat capacity
122　coefficient (γ_e, where the electronic heat capacity is $\gamma_e \times$T) has been experimentally reported to be 10.12
123　mJ/mol-K^2 Marchidan and Ciopec (1976); Schachinger and Lamprecht (1989) , and this value is utilized
124　here to determine the total heat capacity as a function of temperature.

3 RESULTS

3.1 Equilibrium properties of α-U

125

126   The equilibrium lattice constants at 300 K were calculated to be: a = 2.78 Å, b = 5.91 Å, and c = 4.93 Å.
127 These results compare very favorably to the experimental literature (a = 2.85Å, b = 5.87Å, and c = 4.96
128 ÅLawson et al. (1988)), with the largest deviation observed for the a lattice constant at a magnitude of
129 approximately 2.5%. Some deviation is not unexpected, as it has been shown that DFT calculations do
130 not always exactly match the experimental findings, particularly for the lattice constant. However, these
131 results are in accordance with previously computational investigations of α-U performed at 0 K, when
132 thermal expansion is taken into account Huang and Wirth (2011); Beeler et al. (2013). The complete data
133 for equilibrium lattice constants as calculated in this work is included in Table A1.

134   The normalized lattice constants as a function of temperature are shown in Fig. 2. Each lattice constant
135 is normalized to its determined value at 100 K, which is the lowest temperature analyzed. Thermal
136 expansion occurs in both the a and c directions, while thermal contraction occurs in the b direction, as
137 has been previously experimentally observed Touloukian et al. (1975). The recommended directional
138 linear thermal expansion curves from Touloukian et al. (1975) are included as a comparison in Fig. 3.
139 Touloukian summarized 48 individual experiments on both single and polycrystalline samples and provided
140 a recommended tabular fit for each a, b, c, and volumetric thermal expansion. These experiments did not
141 all necessarily quantify their uncertainty, however, Touloukian stated that the recommended values are
142 considered accurate to within +/- 5%. The data in Fig. 3 utilizes 300 K as the reference point for both
143 the AIMD data and the experimental data, and as such, the change in length at 300 K is zero. It can be
144 observed that the AIMD predicted thermal expansion in the a direction is significantly greater than that
145 determined from experiment. Similarly, the amount of contraction in the b direction predicted from AIMD
146 is significantly greater than that observed in experiments. However, the c direction exactly matches the
147 linear thermal expansion determined from experiments. Qualitatively, all of the behaviors are identical,
148 with the a and b directions expressing a more extreme expansion/contraction behavior. The source of the
149 deviations from experiment **is** currently unknown. A comparison of the elastic constants calculated at 0
150 K Beeler et al. (2013)compared to the experimentally determined elastic constants Fisher and McSkimin
151 (1958) yielded no obvious discrepancies that would point to the specific observed trends in the thermal
152 expansion as a function of temperature. The DFT-predicted elastic constants generally overestimate the
153 experimental elastic constants, including all of C_{11}, C_{22}, C_{33}, and the bulk modulus, and do not imply the
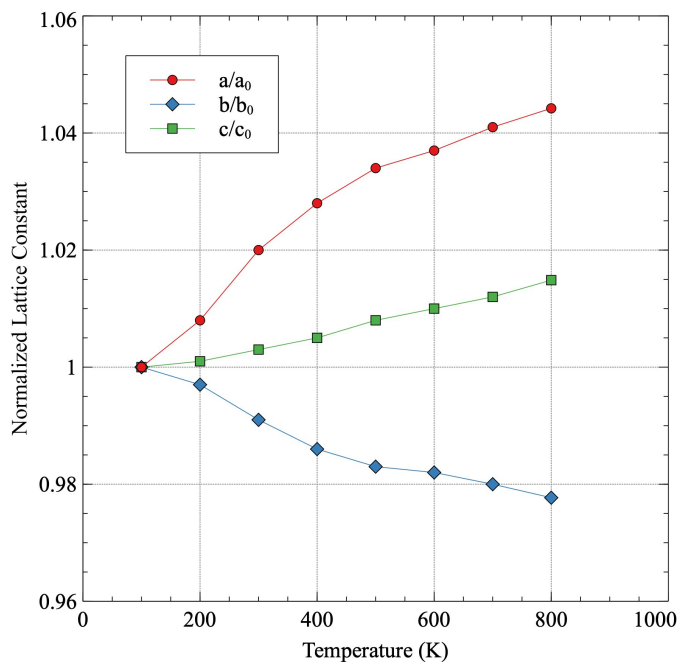154 existence of exaggerated swelling/contraction in the a/b directions.

Figure 2. The normalized lattice constants as a function of temperature for α-U. Each lattice constant is normalized to its value at 100 K.
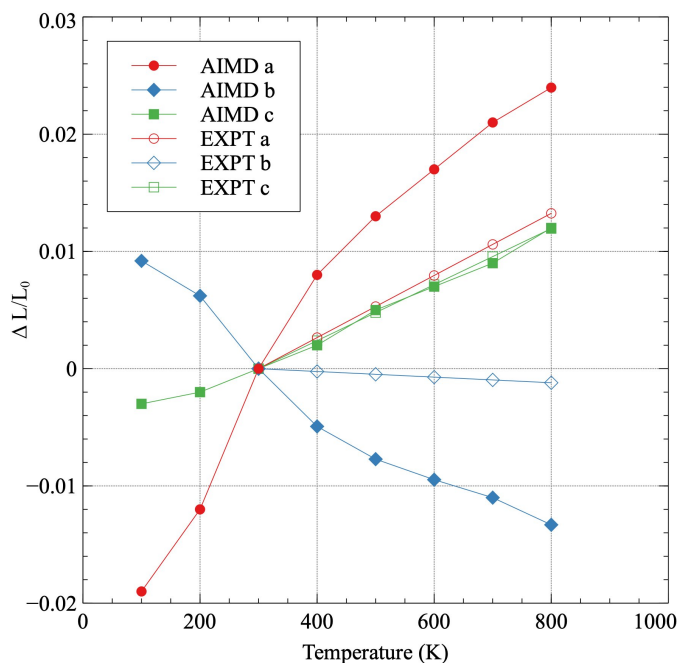

Figure 3. The linear thermal expansion coefficient for each lattice constant in α-U. Thermal expansion is normalized to 300 K, which is the lowest temperature in the experimental data Touloukian et al. (1975).

155   The volume-averaged **linear** thermal expansion is calculated and compared to a different set of
156 experimental results from Touloukian Touloukian et al. (1975) in Fig. 4. **The volume-averaged linear**
157 **thermal expansion utilizes the cube-root of the volume at each temperature of interest.** Interestingly,
158 the data from AIMD nearly exactly matches the experimental results for volumetric-averaged **linear**
159 thermal expansion, with only slight deviations presenting above 600 K. Thus, despite the differences in the

160 individual components of thermal expansion in α-U, which are somewhat substantial, the cumulative effect
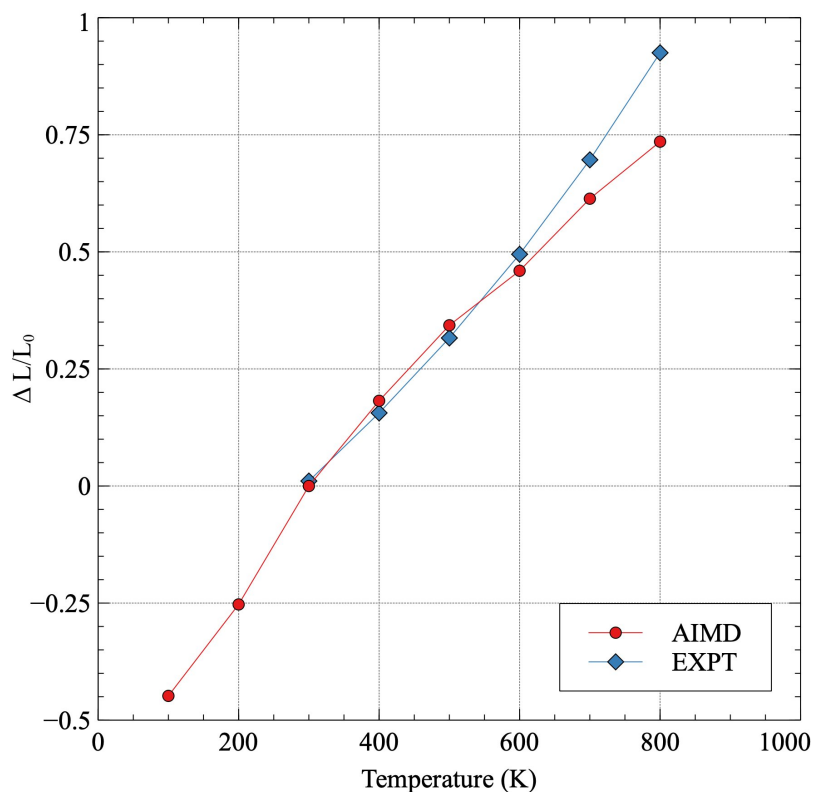161 on total volume expansion reproduces the experimental observations.

Figure 4. Volume-averaged linear thermal expansion in α-U. Thermal expansion is taken with respect to
300 K and compared to experimental results Touloukian et al. (1975).

162   The total constant pressure heat capacity is determined from a summation of equation 3 and the electronic
163 heat capacity contribution as determined by experiments, and is plotted in Fig. 5. The complete heat capacity
164 data as calculated in this work is included in Table A2. Data points are shown at intermediate temperatures,
165 as the formalism in equation 3 assumes effectively a constant value of C_p over the temperature range.
166 Thus, utilizing data points at 100 K and 200 K, for example, yields a value of C_p at 150 K in this work.
167 Experimental data is only reported for room temperature and upwards, and the agreement with the AIMD
168 is generally excellent. The maximum deviation is observed at 750 K, where the AIMD results under-predict
169 the magnitude of C_p by approximately 11%. At lower temperatures, the deviation can be less than 5%. Thus,
170 while the magnitude of the heat capacity is generally the same, it appears that the experimentally observed
171 heat capacity is more sensitive to temperature, showing a total change from 250-750 K of 17 J/mol-K,
172 while AIMD only predicts **an** increase of 11 J/mol-K over this temperature range. **Sources of error**
173 **between the experimental measurements and computational calculations can include impurities in**
174 **the material, effects from underlying microstructure, defect concentrations, inaccuracies in the**
175 **fundamental computational theories, etc. Thus, while there is not exact agreement over the entire**
176 **temperature range, the correlation between the AIMD results and experiment is considered quite**
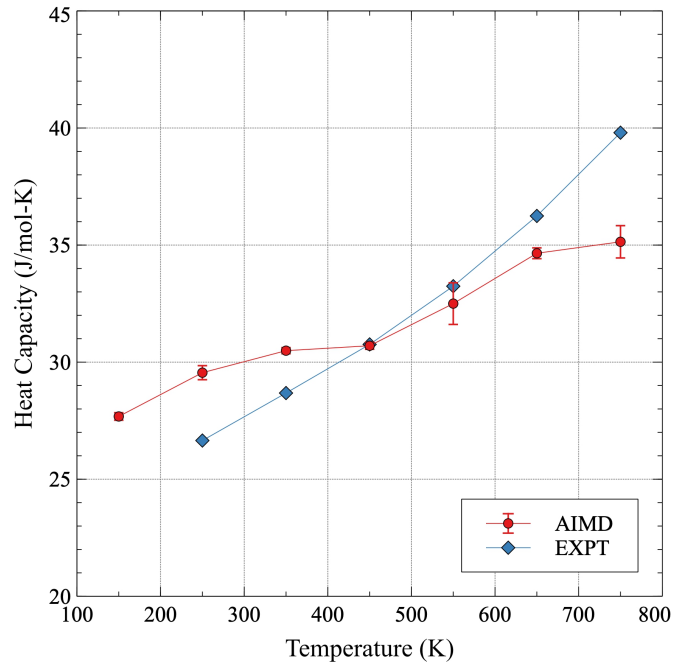177 **good.**

Figure 5. The constant pressure heat capacity of α-U from 100 K to 800 K. Results from this work are compared to experimental results from Konings Konings and Benes (2010). Error bars indicate twice the standard error of the AIMD dataset.

3.2 Point defects in α-U

The point defect formation energy of interstitials and vacancies in α-U is shown in Fig. 6 and included in Table A3. The defect formation energy for both types of defects tends to slightly decrease with increasing temperature until approximately 400 K. Above 400 K, an increase in the defect formation energy with increasing temperature is observed. The relative magnitudes of the defect formation energies with respect to one another are **near-constant** across the entire temperature range investigated, with the average interstitial formation energy (3.4 eV) about 2.3 times the average vacancy formation energy (1.46 eV). Error bars shown in Fig. 6 are twice the standard error, where the standard error for formation energies is defined as

$$SE = \sqrt{\frac{\sigma_{\mathbf{bulk}}}{\sqrt{\mathbf{N}}} + \frac{\sigma_{\mathbf{def}}}{\sqrt{\mathbf{N}}}} \tag{4}$$

where $\sigma_{bulk/def}$ is the standard deviation of the dataset utilized for determining the average energies of either the defect-free or the defected system, and N is the sample size, which is ten simulations for both the defected and defect-free simulations. The standard error in the data set tends to increase with increasing temperature, as would be expected. The results from the lower temperature regime can be compared to previous results from 0 K DFT calculations. At 100 K, the interstitial formation energy is found to be 3.81 eV, and the vacancy formation energy is found to be 1.69 eV. These results compare favorably to previous 0 K DFT results Huang and Wirth (2011), which showed a vacancy formation energy of 1.69 eV (an exact match), and interstitial formation energy of 4.42 eV. That the interstitial formation energy from this work is lower is not unsurprising. While DFT can access any prescribed positional state, the identification of the lowest energy defect location can often be complex and is complicated by the possibility of local minima. By including temperature effects, atomic vibrations can more readily overcome any potential local minima that exist within the energy surface, theoretically finding the lowest possible energy state, and

198 thus the equilibrium defect location at that given temperature. This data can be utilized to conduct higher
199 length scale simulations **that** attempt to describe defect formation and mobility and those which include an
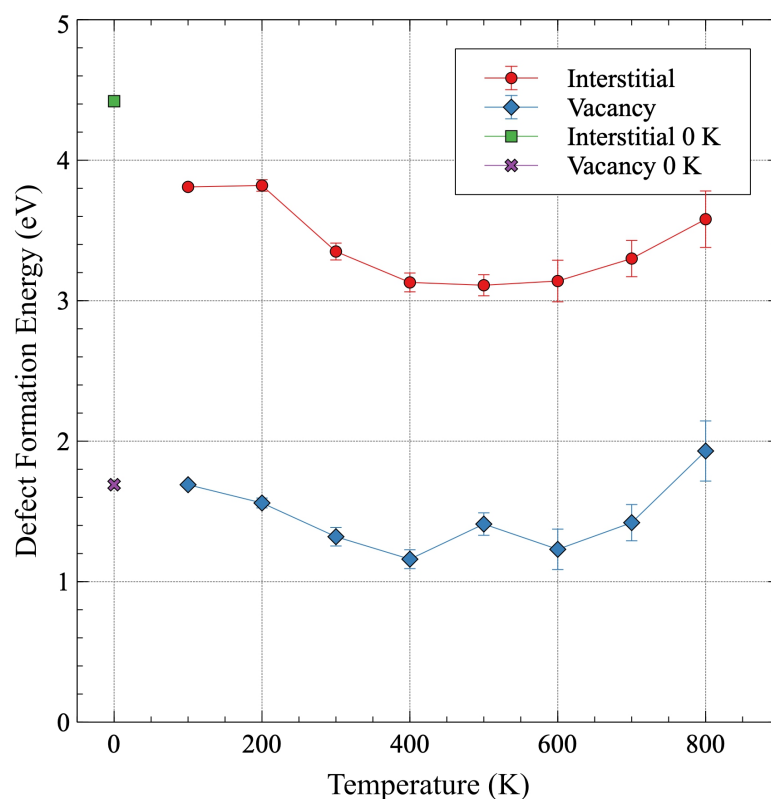200 estimation of the equilibrium concentrations of defects.

Figure 6. The formation energy of an interstitial and a vacancy in α-U as a function of temperature. The defect formation energies from previous DFT work are included for comparison Huang and Wirth (2011).

201   The introduction of a defect and relaxation in an NpT ensemble allows for the analysis of volume changes
202 due to individual point defects. These volume changes are reported as a function of temperature in Fig.
203 7, with error bars included as twice the standard deviation of the dataset. The defect-induced strains are
204 also included in Table A4. For interstitials, there exist two distinct regimes in the defect-induced strain
205 environment, with 400 K serving as the demarcation temperature. Below 400 K, strain is relatively large and
206 positive (lattice expansion) in the *a* direction, and relatively large and negative (lattice compression) for the
207 *b* direction. The magnitudes of those strains decrease with increasing temperature up to 400 K, above which
208 they maintain a relatively fixed value, with some statistical fluctuation. It is unknown whether the deviation
209 at 600 K is due to some distinct behavioral changes, or is simply the result of thermal noise. However, data
210 points at 600 K generally remain within the general trend of the dataset. The *c* lattice constant exhibits
211 very slight positive strain across the entire temperature range, with no obvious changes in behavior. For
212 vacancies, the general magnitude of the strain is significantly less than that observed for interstitials, with
213 the maximum strain of -0.5% observed at 800 K for the *b* lattice constant. While it is more difficult to
214 discern trends in the vacancy strain as a function of temperature, several pieces of information can be
215 readily extracted. The *c* lattice constant displays no observed strain from vacancies at any temperature. For
216 the *a* and *b* lattice constants, opposite trends present themselves above 400 K, in that the *a* lattice constant
217 strain increases with increasing temperature and the *b* lattice constant strain decreases with increasing
218 temperature. In a general sense, the strain behavior of defects is as expected, in that interstitials yield

219　a lattice expansion, while vacancies produce lattice contraction. However, the manner in which those
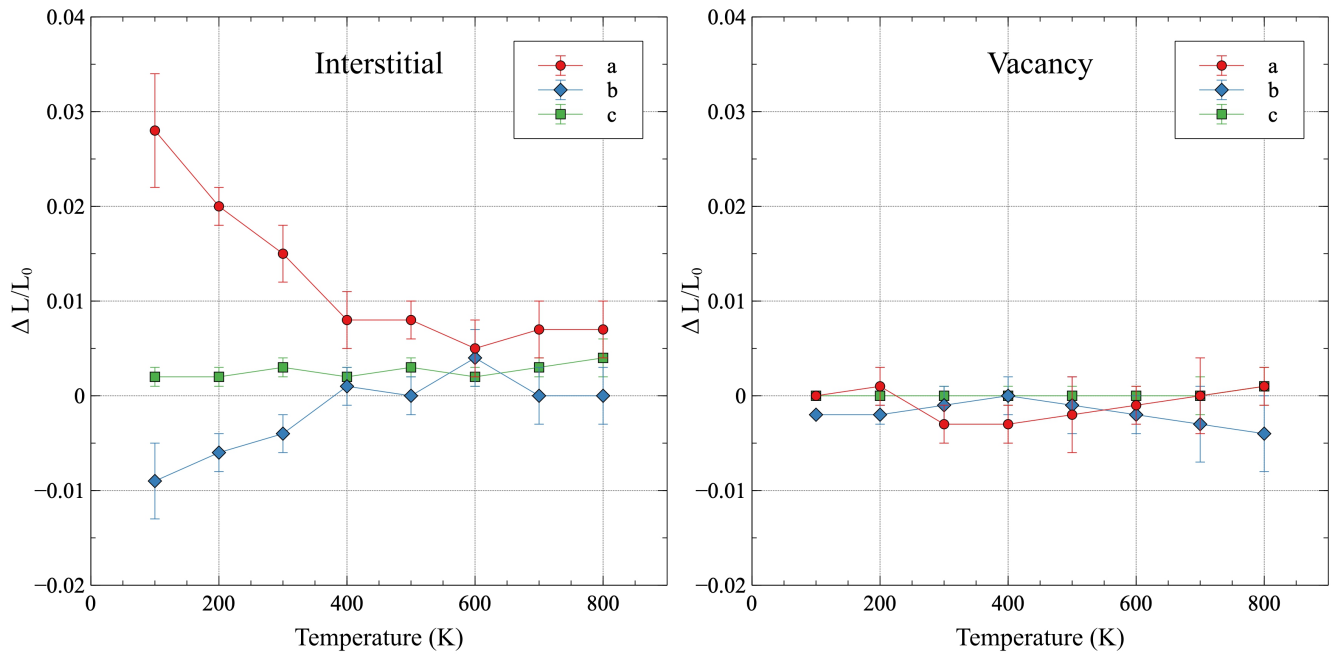220　volumetric averages are produced is quite complex and is significantly **temperature-dependent**.

Figure 7. The lattice strain induced from an interstitial or vacancy in α-U as a function of temperature, taken with respect to the equilibrium volume at that given temperature. Error bars indicate twice the standard deviation of the dataset.

4　DISCUSSION

221　This work indicates **several** lattice and volume effects that are strongly dependent upon the temperature
222　of the system. Excepting the heat capacity, all of these calculated properties seem to indicate two regions
223　of behavior, one below 400 K and one above 400 K. Also, it should be re-emphasized that the heat
224　capacity utilized an experimental data point for the determination of the electronic heat capacity. Thus,
225　from the purely computationally obtained data, there are differences in lattice constant, defect-induced
226　lattice strain, and defect formation energy, in these two temperature regimes. To briefly summarize, thermal
227　expansion/contraction in the *a*/*b* direction occurs rapidly from 100 K up to 400 K, after which a more linear
228　and gradual change in the lattice constant takes place. Defect formation energies decrease in magnitude up
229　to 400 K, above which they tend to slightly increase. Defect lattice strains for interstitials decrease/increase
230　in the *a*/*b* direction up to 400 K, above which they maintain essentially the same magnitude. A similar
231　trend in defect lattice strains for vacancies is present, but the magnitude is significantly less and potentially
232　swamped by thermal fluctuations, and thus the statistical certainty of the finding is reduced.

233　　In an attempt to identify underlying changes in the atomic and electronic structure as a function of
234　temperature, two additional analyses were performed. The first was a coordination analysis, in which the
235　radial distribution function (rdf) was constructed for a snapshot of the equilibrated α-U structure at 100 K,
236　400 K, and 800 K. If a modification in the bond lengths is occurring that can yield differences in structure,
237　such a modification would present itself as peak shifts in the rdf. This coordination analysis is presented in
238　Fig. 8, but yielded no discernible trends, and the general bond length and peak broadening **confirm** what is
239　observed in Fig. 2 and Fig. 3 outlining thermal expansion. Specifically, there is general peak broadening

240   with temperature, and the second nearest neighbor peak (in the *b* direction) slightly shifts towards a smaller
241   distance. The second analysis involved the electronic density of states (DOS). If the character of valence
242   electrons participating in the bonding **is** changing as a function of temperature, the electronic DOS would
243   identify such changes, and the electronic DOS is known to slightly change as a function of the phase
244   of uranium Beeler et al. (2013). The electronic DOS was calculated, and only minimal variation in the
245   electronic structure was observed as a function of temperature. There was no indication that two regions of
246   electronic structure behavior exist for the α phase. Due to the lack of identifiable structure variation as a
247   function of temperature, likely due to statistical noise in the sampling. These results are not displayed here,
248   as the DOS can be obtained from the literature Beeler et al. (2013); Hood et al. (2008). The underlying
249   cause of the apparent two-region behavior is unclear and warrants further computational investigation, in
250   addition to experimental studies on high-purity uranium to either confirm or refute the findings in this work.
251   It should be emphasized that these results are statistically significant, but are still susceptible to inherent
252   errors in the modeling methodology, such as the inability for DFT to predict the lattice and elastic constants
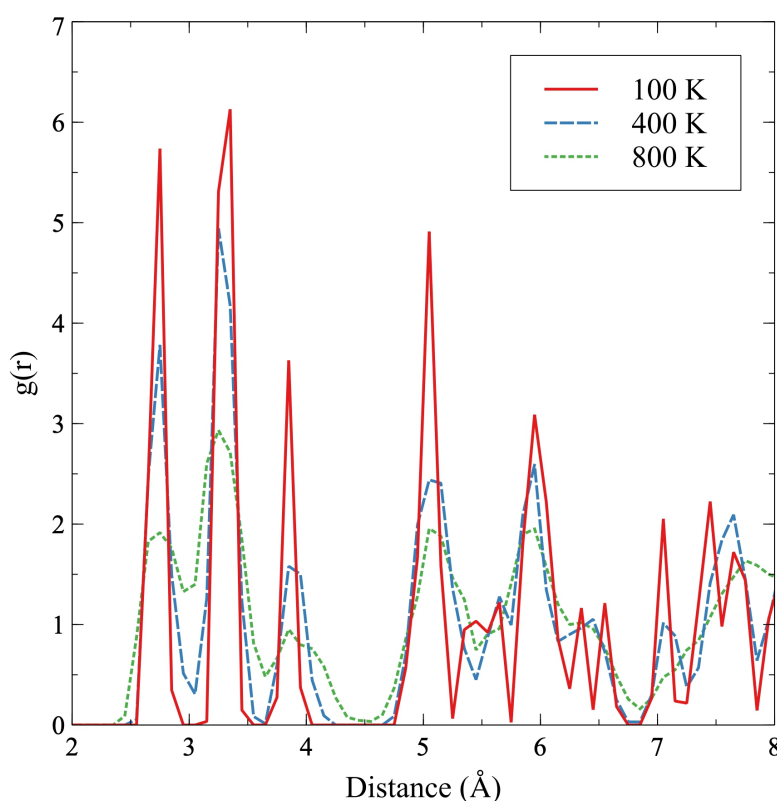253   of α-U with sufficient accuracy at 0 K.

Figure 8. The radial distribution function in α-U at 100 K, 400 K, and 800 K.

254   This work has identified that individual point **defects** can produce somewhat significant lattice strain, but
255   it is unknown if such point defects could be responsible for experimentally observed macroscopic shape
256   change. Comparison of the calculated direction of the defect-induced strains to the experimental literature
257   on irradiation growth provides contradictory information. Paine and Kittel Paine and Kittel (1958) and
258   Loomis and Gerber Loomis and Gerber (1968) both investigated dimensional change of **single-crystal**
259   uranium under irradiation. Their findings were in general agreement with one another, and showed a
260   contraction of the bulk crystal in the *a* direction, an expansion in the *b* direction, and no change in the *c*

261 direction. While the AIMD results of point defect-induced strains presented here agree with the lack of
262 dimensional change in the c direction, exactly the opposite behavior is observed in Fig. 7 for the a and b
263 directions. This work showed that interstitials are the dominant strain inducers, producing expansion in the
264 a direction and contraction in the b direction. Due to the relatively large induced strains from interstitials,
265 it is expected that these types of point defects would display strongly anisotropic diffusion. Given that
266 isolated point defects lead to the opposite trends from those observed experimentally, it is possible that
267 defect clusters or defect loops display different strain behaviors than individual point defects, and are the
268 features responsible for irradiation growth in α-U. Such research is beyond the scope of AIMD, which is
269 currently sufficiently computationally expensive to exclude the possibility of analysis of extended defects.
270 Thus, classical molecular dynamics simulations can be performed and validated against the work presented
271 here. Ideally, in addition to further computational studies, the experimental results from over sixty years
272 ago should be reproduced and modern characterization methods applied to extract fundamental defect
273 populations, densities, and orientations.

5 CONCLUSIONS

274 In this study, AIMD simulations were performed to calculate temperature-dependent properties of the
275 α phase of U from 100 K to 800 K. The thermal expansion of each lattice constant was analyzed and
276 compared to the experimental literature. Although the general direction of thermal expansion corresponded
277 to the experimental findings (positive in a and c, negative in b), the magnitudes of coefficient of thermal
278 expansion for the a and b directions was greater than that observed experimentally. However, the volumetric
279 expansion corresponded nearly exactly to the experimental findings in the literature. The heat capacity
280 was calculated as a function of temperature and showed a general agreement with experimental results,
281 although the computationally determined heat capacity was slightly less sensitive to temperature. Variation
282 in point defect formation energies was determined, with an average interstitial formation energy of 3.40
283 eV, and an average vacancy formation energy of 1.46 eV, over the entire temperature range. Lattice strains
284 resulting from point defects were determined, showing that interstitials induce significantly more strain than
285 vacancies, and the nature of that strain is highly dependent on the individual lattice directions, where the a
286 direction expands and the b contracts due to the introduction of an interstitial. Finally, all of these results
287 seem to indicate a two-region behavior, with the transition at 400 K. The thermal expansion/contraction in
288 the a/b direction occurs rapidly from 100 K up to 400 K, after which a more linear and gradual change in
289 the lattice constant takes place. Defect formation energies decrease in magnitude up to 400 K, above which
290 they tend to slightly increase. Defect lattice strains for interstitials decrease/increase in the a/b direction up
291 to 400 K, above which they maintain essentially the same magnitude. Coordination and electronic structure
292 investigations provided no insight into the possible cause of this potential transition in behavior.

293 This work has shown that isolated point defects cannot be the primary driving force responsible for the
294 significant **irradiation-induced** growth of α-U observed experimentally. This work can be utilized as the
295 basis for mesoscale simulations that take into account defect populations, defect diffusion, and defect strain
296 behaviors. It is emphasized that additional computational work utilizing classical molecular dynamics
297 on extended defects should be performed, in addition to experimental irradiation and characterization, to
298 further elucidate the underlying phenomena governing the interactions of point defects with the α-U crystal
299 structure.

300 5.0.1 Permission to Reuse and Copyright

301 Figures, tables, and images will be published under a Creative Commons CC-BY **license** and
302 permission must be obtained for use of copyrighted material from other sources (including re-
303 published/adapted/modified/partial figures and images from the internet). It is the responsibility of the

304 authors to acquire the licenses, to follow any citation instructions requested by third-party rights holders,
305 and cover any supplementary charges.

CONFLICT OF INTEREST STATEMENT

306 The authors declare that the research was conducted in the absence of any commercial or financial
307 relationships that could be construed as a potential conflict of interest.

AUTHOR CONTRIBUTIONS
ACKNOWLEDGMENTS

6 APPENDIX

316 This appendix includes tabulated data which has been presented and discussed above.

Table A1. The calculated lattice parameter of α-U from 100 K to 800 K.

Temperature (K)	a_0 (Å)	b_0 (Å)	c_0 (Å)	V/at ($Å^3$)
100	2.72	5.96	4.91	79.75
200	2.74	5.94	4.92	80.22
300	2.78	5.91	4.93	80.83
400	2.80	5.88	4.94	81.27
500	2.82	5.86	4.95	81.67
600	2.82	5.85	4.96	81.95
700	2.83	5.84	4.97	82.33
800	2.84	5.83	4.98	82.63

Table A2. The calculated constant pressure heat capacity of α-U from 100 K to 800 K, compared to experimental values from Konings and Benes (2010). Units in J/mol-K.

Temperature (K)	AIMD	Reference
150	27.7	-
250	29.5	26.7
350	30.5	28.7
450	30.7	30.8
550	32.5	33.2
650	34.7	36.2
750	35.1	39.8

Table A3. The interstitial and vacancy formation energy in α-U as a function of temperature. AIMD results are compared to 0 K DFT data (denoted with *) from Huang and Wirth (2011). Units in eV.

Temperature (K)	Interstitial	Vacancy
0*	4.42	1.69
100	3.81	1.69
200	3.82	1.56
300	3.35	1.32
400	3.13	1.16
500	3.11	1.41
600	3.14	1.23
700	3.30	1.42
800	3.58	1.93

Table A4. The defect-induced strain from interstitials and vacancies as a function of temperature. The strain is defined as $\Delta L/L_0$, where L_0 is the reference length at the given temperature.

Temperature (K)	Interstitial			Vacancy		
	a	b	c	a	b	c
100	0.028	-0.009	0.002	0.000	-0.002	0.000
200	0.020	-0.006	0.002	0.001	-0.002	0.000
300	0.015	-0.004	0.003	-0.003	-0.001	0.000
400	0.008	0.001	0.002	-0.003	0.000	0.000
500	0.008	0.000	0.003	-0.002	-0.001	0.000
600	0.005	0.004	0.002	-0.001	-0.002	0.000
700	0.007	0.000	0.003	0.000	-0.003	0.000
800	0.007	0.000	0.004	0.001	-0.004	0.001

REFERENCES

317 Barrett, C., Mueller, H., and Hitterman, R. (1963). Crystal structure variations in alpha uranium at low
318   temperatures. *Phys. Rev.* 129, 625
319 Beeler, B., Andersson, D., Jiang, C., and Zhang, Y. (2020). Ab initio molecular dynamics investigation of
320   point defects in gamma-u. *J. Nucl. Mater.* 545, 152415
321 Beeler, B., Deo, C., Baskes, M., and Okuniewski, M. (2013). First principles calculations of the structure
322   and elastic constants of alpha, beta and gamma uranium. *J. Nucl. Mater.* 433, 143
323 Beeler, B., Good, B., Rashkeev, S., Deo, C., Baskes, M., and Okuniewski, M. (2010). First principles
324   calculations for defects in U. *J. Phys.: Cond. Mat.* 22, 505703
325 Blöchl, P. (1994). Projector augmented-wave method. *Phys. Rev. B* 50, 17953
326 Bouchet, J. and Bottin, F. (2017). High-temperature and high-pressure phase transitions in uranium. *Phys.*
327   *Rev. B* 95, 054113
328 Castellano, A., Bottin, F., Dorado, B., and Bouchet, J. (2020). Thermodynamic stabilization of γ-u-mo
329   alloys: Effect of mo content and temperature. *Phys. Rev. B* 101, 184111
330 Fisher, E. and McSkimin, H. (1958). Adiabatic elastic moduli of single crystal alpha uranium. *J. Appl.*
331   *Phys.* 29, 1473
332 Hellman, O., Abrikosov, I. A., and Simak, S. I. (2011). Lattice dynamics of anharmonic solids from first
333   principles. *Phys. Rev. B* 84, 180301(R)
334 Hellman, O., Steneteg, P., Abrikosov, I., and Simak, S. (2013). Temperature dependent effective potential
335   method for accurate free energy calculations of solids. *Phys. Rev. B* 87, 104111

336   Hohenberg, P. and Kohn, W. (1964). Inhomogeneous electron gas. *Phys. Rev.* 136, B864

337   Hood, R., Yang, L., and Moriarty, J. (2008). Quantum molecular dynamics simulations of uranium at high
338   pressure and temperature. *Phys. Rev. B* 78, 024116

339   Huang, G.-Y. and Wirth, B. (2011). First-principles study of diffusion of interstitial and vacancy in alpha
340   U-Zr. *J. Phys.: Cond. Mat.* 23, 205402

341   Huang, G.-Y. and Wirth, B. (2012). First-principles study of bubble nucleation and growth behaviors in
342   alpha u-zr. *J. Phys.: Cond. Mat.* 24, 415404

343   Jokisaari, A. (2020). Irradiation-induced internal stresses in polycrystalline alpha-uranium: a mesoscale
344   mechanical approach. *Comp. Mat. Sci.* 176, 109545

345   Kohn, W. and Sham, L. (1965). Self-consistent equations including exchange and correlation effects. *Phys.*
346   *Rev.* 140, A1133

347   Konings, R. and Benes, O. (2010). The thermodynamic properties of the f-elements and their compounds.
348   i. the lanthanide and actinide metals. *Journal of Physical and Chemical Reference Data* 39, 043102

349   Kresse, G. and Fürthmuller, J. (1996a). Efficiency of ab-initio total energy calculations for metals and
350   semiconductors using a plane-wave basis set. *Comput. Mat. Sci.* 6, 15

351   Kresse, G. and Fürthmuller, J. (1996b). Efficient iterative schemes for ab initio total-energy calculations
352   using a plane-wave basis set. *Phys. Rev. B* 54, 11169

353   Kresse, G. and Hafner, J. (1993). Ab initio molecular dynamics for liquid metals. *Phys. Rev. B* 47, 558

354   Kresse, G. and Hafner, J. (1994). Ab initio molecular-dynamics simulation of the liquid-metal-amorphous-
355   semiconductor transition in germanium. *Phys. Rev. B* 49, 14251

356   Kresse, G. and Joubert, D. (1999). From ultrasoft pseudopotentials to the projector augmented-wave
357   method. *Phys. Rev. B* 59, 1758

358   Kruglov, I., Yanilkin, A., Oganov, A., and Korotaev, P. (2019). Phase diagram of uranium from ab initio
359   calculations and machine learning. *Phys. Rev. B* 100, 174104

360   Ladygin, V., Korotaev, P., Yanilkin, A., and Shapeev, A. (2020). Lattice dynamics simulation using machine
361   learning interatomic potentials. *Comp. Mat. Sci.* 172, 109333

362   Lawson, A., Olsen, C., Richardson, J., Mueller, M., and Lander, G. (1988). Structure of beta-uranium.
363   *Acta Crys.* B44, 89

364   Leggett, R., Bierlein, T., and Mastel, B. (1963). *Irradiation behavior of high purity uranium*. Tech. Rep.
365   HW-79559, Hanford Laboratories

366   Lide, D. (2000). *Handbook of Chemistry and Physics: A Ready-Reference Book Chemical and Physical*
367   *Data* (CRC-Press)

368   Lloyd, L. and Barrett, C. (1966). Thermal expansion of alpha uranium,. *J. Nucl. Mater.* 18, 55

369   Loomis, B. and Gerber, S. (1968). Length and electrical resistivity changes of neutron irradiated uranium.
370   *Phil. Mag.* 18, 539

371   Manga, V. and Poirier, D. (2018). Ab initio molecular dynamics simulation of self-diffusion in al–si binary
372   melts. *Modelling Simul. Mater. Sci. Eng.* 26, 065006

373   Marchidan, D. and Ciopec, M. (1976). Enthalpy of uranium to 1500 k by drop calorimetry. *J. Chem.*
374   *Thermo.* 8, 691

375   Matter, H., Winter, J., and Triftshauser, W. (1980). Investigation of vacancy formation and phase
376   transformations in uranium by positron annihilation. *J. Nucl. Mater.* 88, 273

377   Methfessel, M. and Paxton, A. (1989). High-precision sampling for brillouin-zone integration in metals.
378   *Phys. Rev. B* 40, 3616

379   Monkhorst, H. and Pack, J. (1976). Special points for brillouin-zone integrations. *Phys. Rev. B* 13, 5188

380 Paine, S. and Kittel, J. (1958). *PRELIMINARY ANALYSIS OF FISSION-INDUCED DIMENSIONAL*
381 *CHANGES IN SINGLE CRYSTALS OF URANIUM*. Tech. Rep. ANL-5676, Argonne National
382 Laboratory

383 Perdew, J., Burke, K., and Ernzerhof, M. (1996). Generalized gradient approximation made simple. *Phys.*
384 *Rev. Lett.* 77, 3865

385 Perdew, J., Burke, K., and Ernzerhof, M. (1997). Erratum: Generalized gradient approximation made
386 simple. *Phys. Rev. Lett.* 78, 1396

387 Schachinger, L. and Lamprecht, I. (1989). Heat capacity of uranium metal at low temperatures. a
388 reminiscence. *Thermoc. Acta* 151, 203

389 Söderlind, P. (1998). Theory of the crystal structures of cerium and the light actinides. *Adv. in Phys.* 47,
390 959

391 Söderlind, P., Grabowski, B., Yang, L., Landa, A., Bjorkman, T., Souvatis, P., et al. (2012). High-
392 temperature phonon stabilization of ! -uranium from relativistic first-principles theory. *Phys. Rev. B* 85,
393 060301

394 Taylor, C. (2008). Evaluation of first-principles techniques for obtaining materials parameters of alpha
395 uranium and the (001) alpha uranium surface. *Phys. Rev. B* 77, 094119

396 Timko, J., Bucher, D., and Kuyucak, S. (2010). Dissociation of nacl in water from ab initio molecular
397 dynamics simulations. *J. Chem. Phys.* 132, 114510

398 Touloukian, Y., Kirby, R., Taylor, R., and Desai, P. (1975). *Thermophysical Properties of Matter - Thermal*
399 *Expansion: Metallic elements and alloys*, vol. 12 (IFI/Plenu,)

400 Wang, C., Dai, Y., Gao, H., Ruan, X., Wang, J., and Sun, B. (2010). Ab initio molecular dynamics study of
401 fe adsorption on tin (001) surface. *Mat. Trans.* 51, 2005

402 Xiang, S., Huang, H., and Hsiung, L. (2008). Quantum mechanical calculations of uranium phases and
403 niobium defects in gamma-uranium. *J. Nucl. Mater.* 375, 113

404 Yoo, C.-S., Cyun, H., and Soderlind, P. (1998). Phase diagram of uranium at high pressures and
405 temperatures. *Phys. Rev. B* 57, 10359